Nanoscale three-dimensional charge density and electric field mapping by electron holographic tomography

Fengshan Zheng,[*,†,‡] Vadim Migunov,[†,¶] Jan Caron,[†] Hongchu Du,[†,¶] Giulio Pozzi,[†,§] and Rafal E. Dunin-Borkowski[†]

†*Ernst Ruska-Centre for Microscopy and Spectroscopy with Electrons and Peter Grünberg Institute, Forschungszentrum Jülich, 52425 Jülich, Germany*

‡*Spin-X Institute, Electron Microscopy Center, School of Physics and Optoelectronics, State Key Laboratory of Luminescent Materials and Devices, Guangdong-Hong Kong-Macao Joint Laboratory of Optoelectronic and Magnetic Functional Materials, South China University of Technology, Guangzhou 511442, China*

¶*Central Facility for Electron Microscopy (GFE), RWTH Aachen University, Ahornstrasse 55, 52074 Aachen, Germany*

§*Department FIM, University of Modena and Reggio Emilia, via G. Campi 213/a, 41125 Modena, Italy*

E-mail: f.zheng@fz-juelich.de

Abstract

The operation of nanoscale electronic devices is related intimately to the three-dimensional (3D) charge density distributions within them. Here, we demonstrate the quantitative 3D mapping of the charge density and long-range electric field associated with an electrically-biased carbon fibre nanotip with a spatial resolution of

approximately 5 nm using electron holographic tomography in the transmission electron microscope combined with model-based iterative reconstruction. The approach presented here can be applied to a wide range of other nanoscale materials and devices.

Keywords: Charge density, Electric field, Three-dimensional mapping, Electron holography, Tomography

Nanoscale electronic devices such as transistors and light emitting diodes are widely used in high technology applications. In order to improve the working performance of such devices, it is important to understand the relationship between their local electrical properties and the presence of defects, dopants, interfaces and surfaces.[1] For example, the emission performance of electron sources in electron microscopes (in particular field emitters) is determined by geometrical factors, including local shape, curvature and crystallographic orientation.[2–4] In atom probe tomography,[5] the shape, chemistry and defect distribution of a needle-shaped sample determine the electric field around it, influencing the trajectories of field-evaporated ions and affecting the fidelity of reconstructed atom positions.[6] Similarly, tip-enhanced catalytic efficiency is influenced by the shape and species of the tip.[7,8]

Off-axis electron holography[9] in the transmission electron microscope (TEM) is a powerful technique that can be used to map projected and three-dimensional (3D) electrostatic potentials,[10–18] electric fields[19–23] and charge density distributions[24–28] with nm to atomic spatial resolution. 3D electrostatic potentials have been measured from tilt series of electron holographic phase images to study dopant potentials in semiconductors[11,12,14,15] and the morphologies of nanoscale materials[29–31] and 3D electric fields around specimens have been inferred from phase images based on the assumption of rotational symmetry[23,32] or have made use of simple analytical models.[22] Measurements of 3D charge density distributions in materials have also been proposed.[33,34] However, until now only empirical models for charge density distributions within samples have been fitted by comparing simulated projected potentials with experimental phase images, for example by making use of a line-charge model

and the assumption of cylindrical symmetry for reconstruction of the 3D electric field around a metallic atom probe needle.[22]

In general, the use of backprojection-based tomographic reconstruction to study 3D electrostatic potentials and electric fields is complicated by the fact that they are continuous functions that may vary significantly in magnitude within and outside both the specimen and the field of view (FOV). Reconstructions are then affected more significantly by artefacts than when using electron tomography to recover variations in morphology and composition in materials, especially if full 360° rotation cannot be achieved when recording an experimental tomographic tilt series of off-axis electron holograms. If electrostatic fringing fields are present outside the specimen, then direct tomographic reconstructions of potentials and fields are also affected by the so-called perturbed reference wave (PRW) effect in off-axis electron holography.[23,35]

In this paper, we show that these problems can be circumvented by not determining the 3D potential or field directly, but combining electron holographic tomography with model-based iterative reconstruction (MBIR)[28,36] to first determine the 3D charge density in the specimen, *i.e.*, the source of the potential and field. This approach allows *a priori* information, such as the shape of the object, the PRW effect and the influence of charges that are located outside the FOV to be taken into account.[28] It is also more robust to noise and artefacts that originate from the use of a limited tilt range and can provide a quantitative number for the spatial resolution of the reconstructed charge density.[34,36] The reconstructed 3D charge distribution in the specimen can then be used to infer the 3D electrostatic potential and electric field both inside and around the specimen without the artefacts that would be present by reconstructing them from recorded phase images directly.

We illustrate the method through the experimental measurement of the 3D charge density in an electrically-biased C fibre needle that has a long-range electric field outside it with a spatial resolution of approximately 5 nm. As a needle-shaped sample geometry is similar to that present in some nanoelectronic devices, such as semiconducting nanowires, nanoscale

p-n junctions and field emitters,[11,13,15,20,37] we believe that our results will also be useful in these research fields, in particular to understand the relationship between local electrical properties and the presence of defects, dopants, interfaces and surfaces.

A C fibre needle was prepared using a standard focused ion beam (FIB) milling procedure in an FEI Helios Nanolab 460F1 workstation, as described elsewhere in detail.[38] An electrical bias was applied between the needle and a μm-sized Au counter-electrode in the TEM using a Nanofactory scanning tunnelling microscopy TEM specimen holder. Figure 1a shows a low magnification bright-field TEM image of the experimental setup. The length of the C fibre needle is approximately 2.5 μm. The distance between the needle and the Au counter-electrode is approximately 4.5 μm. The diameter of the apex of the needle is approximately 60 nm. A higher magnification bright-field TEM image is shown in Fig. 1b.

As off-axis electron holography is sensitive to contributions to the electrostatic potential from both the mean inner potential (MIP) of the specimen and the applied electrical bias, two tomographic tilt series of electron holographic phase images were recorded over a tilt range of -52° to $+48^\circ$ with a tilt increment of 4°. The first tilt series was recorded without an electrical bias applied to the needle. On the assumption that the needle does not undergo electron-beam-induced charging, these phase images are sensitive only to the projected MIP of the specimen. They can be used to subtract the MIP contribution to the phase from subsequent images recorded at each tilt angle, as well as to reconstruct the 3D shape of the needle. The second tilt series was recorded with +40 V applied between the needle and the counter-electrode. The MIP contribution to the phase was removed by aligning and subtracting corresponding phase images at each tilt angle with and without the electrical bias applied to the needle. Supplementary Fig. 2 contains further details about this procedure.

The spatial resolution of the reconstruction presented below is limited to approximately 5 nm here primarily by the spatial resolution of the TEM and the aperture size used for hologram reconstruction. It can be improved in future studies by choosing an operating mode of the TEM that has higher spatial resolution, by using a larger aperture size for

hologram reconstruction and by using approaches such as double-resolution or phase-shifting holography.[39,40]

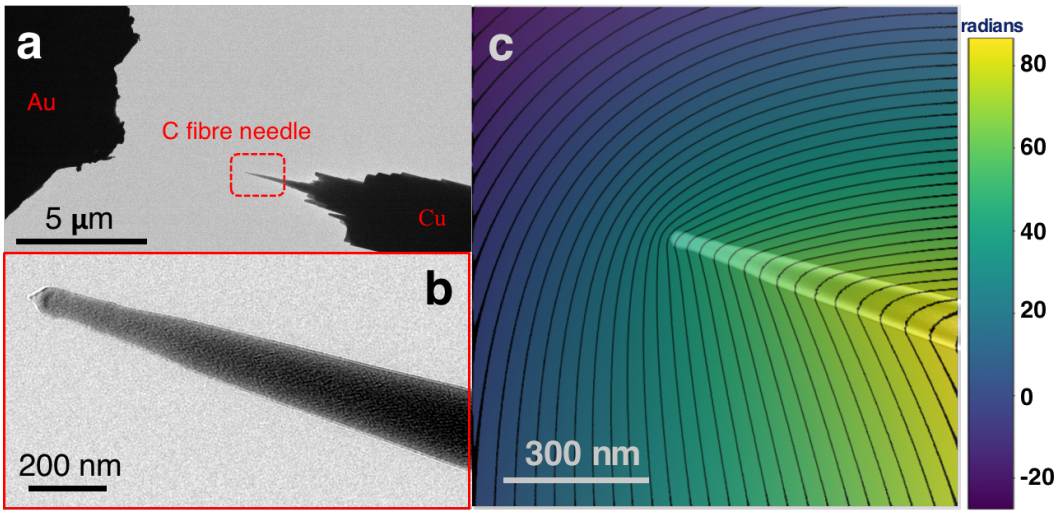

Figure 1: (a) Low magnification bright-field TEM image showing the experimental setup for electrical biasing of a C fibre needle in the TEM. (b) Higher magnification image of the end of the needle. (c) Electron holographic phase difference image with +40 V applied between the needle and the counter-electrode at a 0° sample tilt angle. The mean inner potential contribution to the phase has been removed by subtracting an aligned phase image recorded without a bias applied to the needle. Equiphase contour lines (black) are superimposed. The phase contour spacing is 2π radians. A TEM image of the C fibre needle is overlayed to guide the eye.

Figure 1c shows a resulting phase difference image for a 0° sample tilt angle with equiphase contour lines superimposed. The asymmetry in the contours between the two sides of the needle is a consequence of the PRW effect, *i.e.* the influence on the holographic reference wave of the long-range electric field associated with the voltage applied to the needle. Supplementary Fig. 3 shows similar phase contour images for selected other sample tilt angles. The first dataset alone was used to reconstruct the 3D shape of the needle using the ASTRA toolbox.[41] (See Supplementary Fig. 4 for further details).

3D reconstruction of the charge density in the electrically-biased needle was carried out by applying the MBIR approach[28,36] to the aligned tomographic dataset of phase difference images (after removal of the MIP contribution to the phase at each tilt angle). The 3D shape of the needle (reconstructed from the first dataset) was used to define the volume in

which charges can be placed during reconstruction, on the assumption that no charges are present in the vacuum region around the needle. A buffer region of voxels was also defined immediately outside the 3D reconstruction volume. This buffer region was also allowed to contain "artificial" charges, which are used to represent contributions from the PRW and from charges that are located outside the FOV. These charges can be removed after reconstruction when analysing the charges in the needle alone. By varying the positions and magnitudes of the charges in the reconstruction volume and using them to obtain predicted phase images, the algorithm attempts to minimise the residual with the experimental phase difference images at each sample tilt angle. At the same time, it uses a Euclidean norm for regularisation. This choice favours a solution that minimises the norm of the charge density. In a conductor, charges are expected to be located on the specimen surface. Here, the total of the norm of the charge density is a measure of the total electrostatic potential energy.[42] Therefore, the algorithm converges to a solution that corresponds to a minimum in electrostatic energy. To an extent, this approach guarantees the physical uniqueness of the solution. A compromise between the two criteria is implemented by using a standard L-curve analysis. An optimized parameter for the regularisation is chosen, in order to balance the residual error between the experimental and reconstructed phase measurements and the minimum of the Euclidean norm of the reconstructed charges. Further details are available in Supplementary Fig. 5 and elsewhere.[28,36]

Figure 2a shows a visualisation of the resulting reconstructed 3D charge density in the C fibre needle. As expected, the charge density is greatest at the apex of the needle, which has the highest curvature and is closest to the Au counter-electrode. The maximum charge density is 2.94×10^{18} cm^{-3}. The charge is distributed asymmetrically around the needle, which is not perfectly circular in cross-section. Such an effect can also originate from the reconstruction algorithm if the mask that defines the sample surface is not chosen correctly or if the boundary buffer voxel approach that is used to represent charges outside the FOV and the PRW effect does not work effectively. We therefore verified the result by evaluating the

influence on the reconstructed charge density of changing the size of the 3D mask manually, as well as changing the thickness of the buffer region from 8 to 16, 32 and 64 voxels.

Selected slices extracted from the reconstructed 3D charge density distribution are shown in Figs 2b-f. The xy plane (Fig. 2b) reveals an asymmetry in the charge density (white arrow "1"), which is absent in the yz plane (Fig. 2c) and may be associated with local differences in the shape of the needle. The fact that the majority of the charge is located close to the surface of the needle is visible in the yz plane (Fig. 2c). On the one hand, this observation is consistent with the prediction (based on classical electrostatics) that charges reside on the outer surface of a conductor.[42] On the other hand, it is surprising that the charge penetrates several tens of nm into the surface, perhaps because the needle has a disordered or poorly conducting surface layer. As the spatial resolution of our method is currently about 5 nm, it does not provide unambiguous information about field penetration, band bending or screening depth.[43] This information should be accessible in the future when the spatial resolution of the technique is improved.

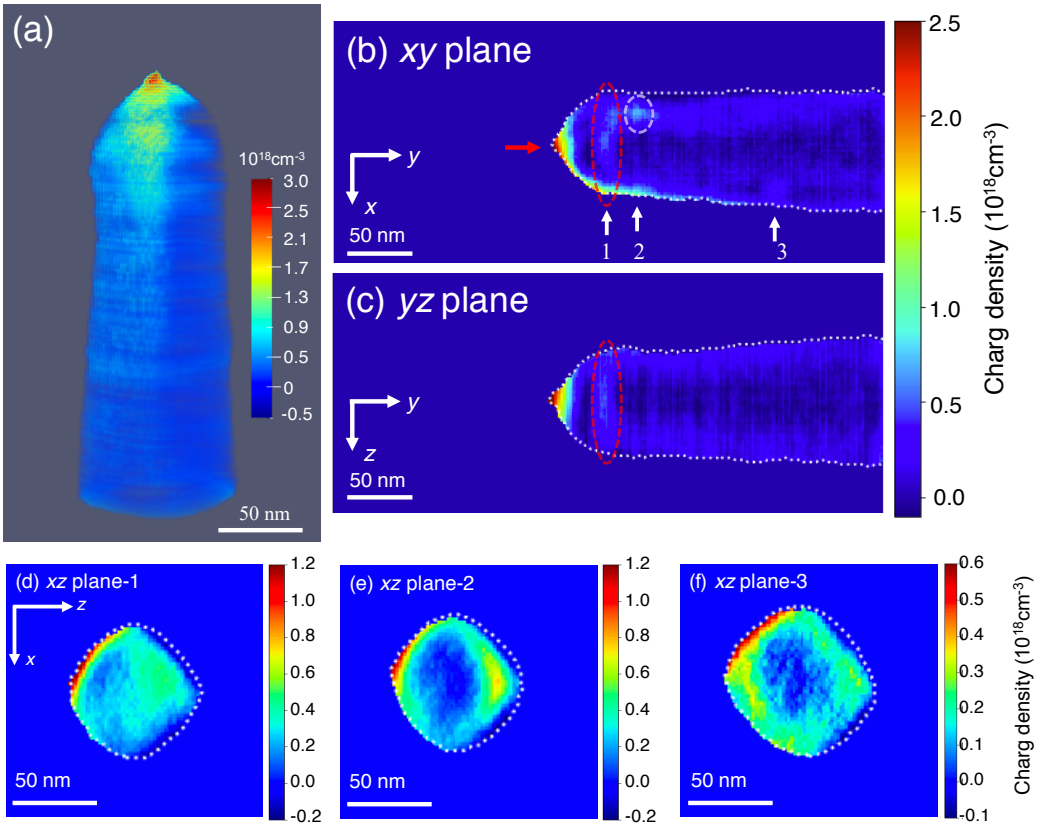

Figure 2: Visualisation of 3D charge density in a C fibre needle reconstructed using electron holographic tomography and the MBIR approach. The needle is biased at +40 V with a distance of 4.5 μm from a Au counter-electrode. (a) Side view of the 3D charge density. (b, c) 2D slices of charge density in the (b) xy and (c) yz planes, extracted from the 3D reconstructed charge density shown in (a). (d-f) Three representative slices of charge density in the xz plane extracted from the 3D reconstructed charge density shown in (a). The positions of the planes are marked by white arrows and numbers in (b). The white dashed lines mark the outline of the needle. See text for details.

A region with a local increase in charge density is marked by red dashed ellipses in Figs 2b-c. It may be associated with a local difference in damage to the needle during sample preparation (*e.g.*, Ga^+ bombardment). Figures 2d-f show three representative xz planes (labelled in Fig. 2b), in which the charge can be seen to be located primarily at the surface of the needle. Plane "1" is thought to lie at the interface between a more insulating apex region and the more conductive shank of the needle. Plane "2" intersects a local maximum in charge density (marked by a white dashed ellipse in Fig. 2b). Plane "3" corresponds to a plane that is at a greater distance from the apex. In planes "2" and "3",

the charge is localised at the outer surface of the needle.

Corresponding charge density profiles determined from the 3D reconstruction are shown in Fig. 3. Figure 3a shows a line profile of the charge density in the xy plane along the axis of the needle (marked by a red arrow in Fig. 2b). In addition to a maximum at the apex, there is a local maximum with a charge density of approximately 0.5×10^{18} cm^{-3}. The charge density along the axis of the rest of needle is close to zero. For the three chosen xz planes, line profiles of the measured charge density are plotted in the z and x directions in Figs 3b-c, respectively. In the z direction (Fig. 3b), the green and blue profiles from planes "2" and "3" are almost symmetrical with respect to the needle axis. The red profile from plane "1" is higher than those from planes "2" and "3" on the axis of the needle. In the x direction (Fig. 3c), the red profile from plane "1" is again higher on the axis of the needle than the other two profiles. It should be noted that negative values in the reconstructed charge distribution fall within the errors that are present due to noise from the experimental data and the reconstruction.

The cumulative charge integrated along the length of the needle, which is shown in Fig. 3d, follows an almost linear trend, suggesting that the line charge density along the needle is almost constant, as expected from analytical solutions.[21,35] The slope of the cumulative charge profile is slightly greater close to the apex of the needle than in the shank, indicating a greater line charge density in this region, perhaps because of its more insulating character or because of a local deviation from an ellipsoidal geometry.[44]

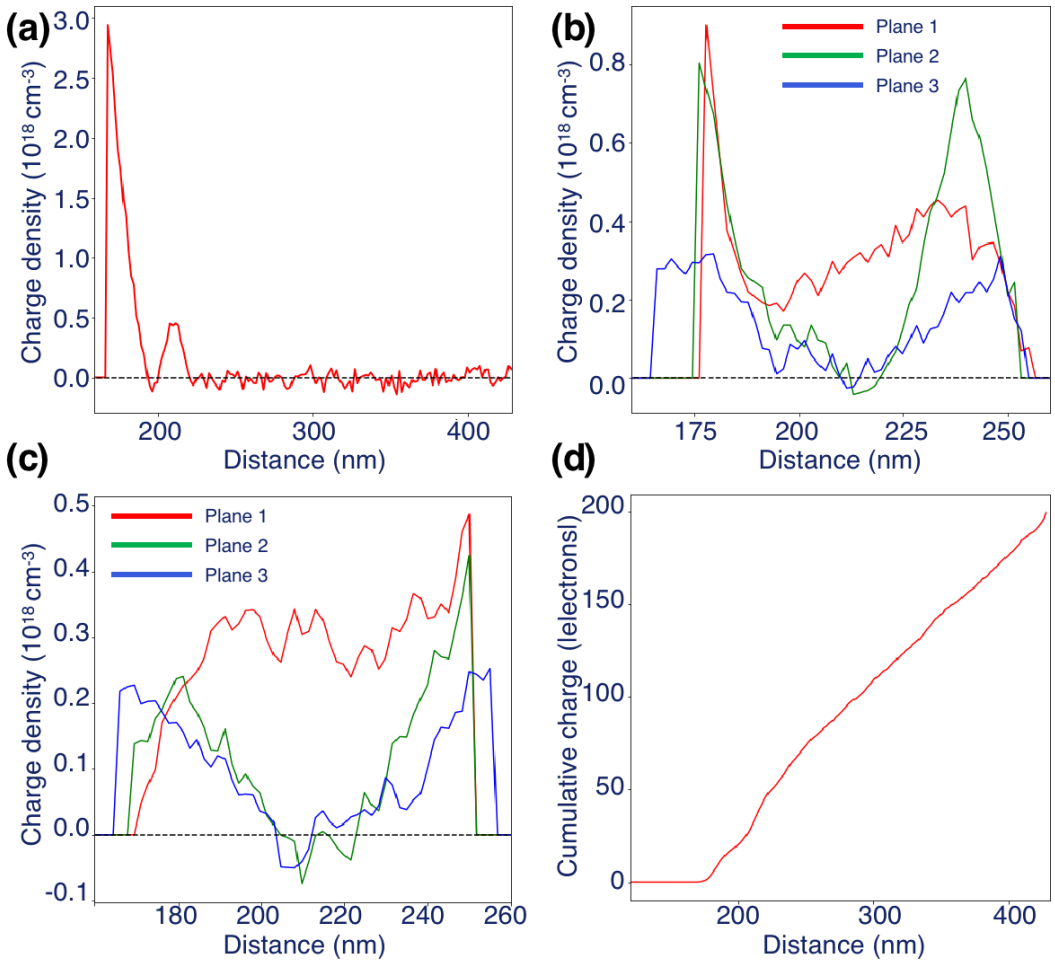

Figure 3: Line profiles of charge density extracted from the 3D charge density shown in Fig. 2 (a) along the axis of the needle (y) in the central xy plane (marked by a red arrow in Fig. 2b) and (b, c) along z and x in three different xz planes (1-red, 2-green, 3-blue) marked in Fig. 2b. (d) Cumulative charge profile along the length of the needle.

The 3D electrostatic potential and electric field can be calculated from the 3D reconstructed charge density by removing the artificial charges in the buffer voxel region and assuming that image charges in the counter-electrode can be defined to have a norm vector with respect to the apex of the needle of $(0, \ -4.5, \ 0)$ μm, as determined from the experimental setup (Fig. 1b). It should be noted that charges outside the FOV also contribute to the electrostatic potential and electric field inside the FOV. However, as the electric field decays in a quadratic manner with distance and the charge density in the needle is negligible far from the apex (see Fig. 3d), it is reasonable to assume that charges outside the FOV

have a negligible contribution in this setup. This consideration is not in conflict with simulations performed by the atom probe community (*e.g.*[45,46]), as we are focusing here only on the local electric field within the FOV, whereas additional boundary conditions in an atom probe apparatus (further from the tip of the needle) affect ion trajectories to the detector.

Figure 4a show a 3D visualisation of the magnitude of the electric field, while Figs 4b-c show slices of the magnitude of the electric field in the central xy and yz planes. The electric field is almost symmetrical about the needle axis. Residual slight asymmetry results from the asymmetry in the reconstructed charge density (as seen in the xy plane in Fig. 4b). Figures 4b-c show that the electric field is strongest close to the apex and that it decays rapidly into the vacuum region with increasing distance from it. The maximum electric field strength measured in the present study is approximately 0.25 GV/m. Based on a single projection model[6] used by the atom probe community, the geometric field factor here is predicted to be approximately 5.33, which falls within theoretical values that typically range between 2 and 14.[46] It should be noted that this factor is highly dependent on the radius and shape of the tip and on the distance to the counter-electrode. Inside the needle (Figs 4b-c), the magnitude of the electric field is strongest in the region close to the surface, where it is thought to be less conducting.

A combination of a streamline plot of the electric field and the electrostatic potential in the central xy plane is shown in Fig. 5. The fact that the field lines are normal to the surface of the needle close to its apex suggests that charges outside the FOV do not influence the reconstruction in this region and that the electric field around the apex can be calculated reliably using the MBIR approach. In contrast, the field lines on the right of the image (close to the shank of the needle) are inclined with respect to the surface of the needle as a result of the influence of missing contributions to the electric field from charges outside the FOV.

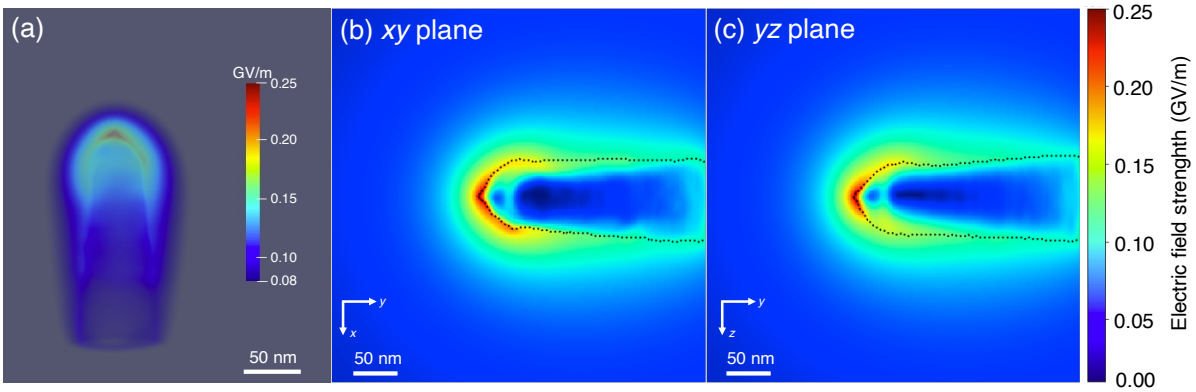

Figure 4: 3D electric field determined from the reconstructed 3D charge density shown in Fig. 2 for the electrically-biased C fibre needle. (a) Magnitude of the electric field plotted on a logarithmic scale. (b, c) Magnitude of the electric field in the central xy and yz planes, respectively. The black dashed line shows the outline of the needle.

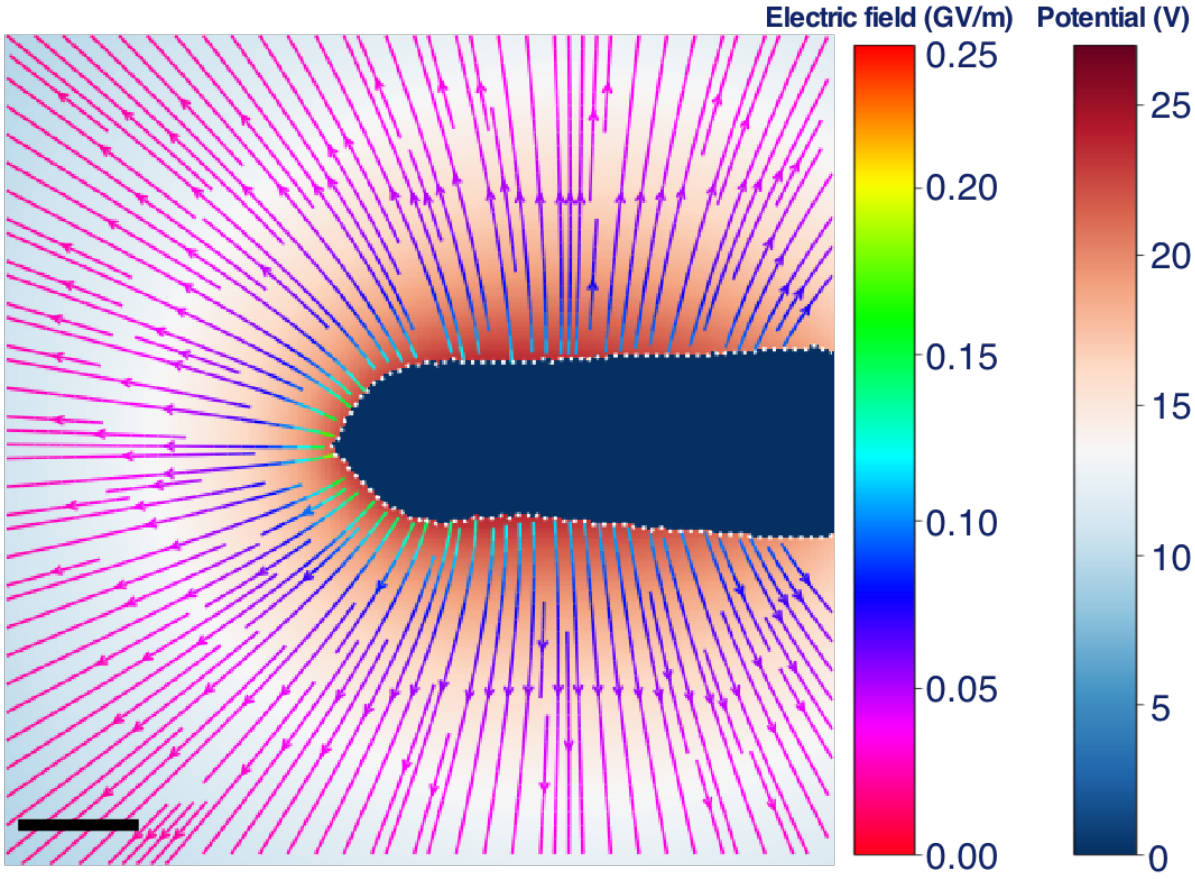

Figure 5: Combination of a streamline plot of the electric field and a plot of the electrostatic potential in the central xy plane of the reconstructed volume of the C fibre needle. The interior of the needle is marked in blue. The scale bar is 50 nm.

In summary, the 3D charge density, electrostatic potential and electric field of an electrically-biased C fibre needle have been determined experimentally using electron holographic tomography combined with model-based iterative reconstruction of the charge density. Tomographic tilt series of holographic phase images with the needle biased at +40 V with respect to a Au counter-electrode were used as input for the algorithm after subtracting the MIP contribution to the phase from each image in the tilt series. The reconstructed charge density is greatest at the apex of the needle and localised primarily close to its surface. The cumulative charge displays a close-to-linear behaviour, which is consistent with a line charge density that is almost constant along the needle. Asymmetry in the reconstructed charge density results from changes in the local geometry of the needle or damage from FIB sample preparation. The 3D electric field and electrostatic potential can be calculated from the reconstructed 3D charge density based on an assumption for the positions of image charges in the Au counter-electrode. The inferred electric field and electrostatic potential are both almost symmetrical about the needle axis. The strength of the electric field is greatest close to the apex of the needle and has a maximum value of 0.25 GV/m at an applied bias voltage of +40 V with a distance of 4.5 μm to the Au counter-electrode. The results suggest that this approach can be used for 3D characterisation of charge, electrostatic potential and electric field from limited datasets recorded from a wide range of nanostructures and may provide guidance for designs and improvements of nanoscale electronic devices.

Methods

C fibre. A high-strength C fibre (T1000) was obtained from Toray company (www.toray.jp). The fibre comprised primarily C ($\geq$ 99%), with a small amount of N, in the form of a highly-textured structure along the fibre axis, with turbostratic graphene as the basic structural unit.[47] This choice of material reduces the influence of changing diffraction conditions during tomographic tilt series acquisition.

Off-axis electron holography. An FEI Titan G^2 60−300 TEM equipped with an ultra-bright field emission electron gun (X-FEG) and two electrostatic biprisms was used for off-axis electron holography experiments. The operating voltage was set to 300 kV. In order to obtain a large field of view, experiments were carried out in Lorentz mode with the conventional microscope objective lens switched off. A scanning tunnelling microscopy TEM specimen holder (Nanofactory Instruments) was used for electrical biasing experiments. Off-axis electron holograms were recorded using an exposure time of 6 s on a 4k × 4k direct electron counting Gatan K2 IS camera. A representative hologram is shown in Supplementary Fig. 1. The holographic interference fringe spacing was approximately 1.7 nm and the interference width was approximately 1.8 μm. 30 holograms were recorded at each tilt angle to increase the signal-to-noise ratio. Reference holograms were recorded from a region of vacuum with the specimen removed from the field of view. Real-space phase and amplitude images were reconstructed from recorded electron holograms with a standard fast Fourier transform algorithm using Holoworks software (Holowerk LLC).

Acknowledgement

The authors thank Prof. Michael Farle and AG Farle at the University of Duisburg-Essen for technical help, Shasha Wang and Prof. Haifeng Du for focused ion beam preparation of the specimen and Werner Pieper and Rolf Speen for technical assistance. The authors acknowledge the European Union for funding through the Marie Curie Initial Training Network SIMDALEE2 (Marie Curie Initial Training Network (ITN) Grant No. 606988 under FP7-PEOPLE-2013-ITN). V. M. and H. D. thank the Deutsche Forschungsgemeinschaft for funding within the framework of the SFB 917 project Nanoswitches. R. D.-B. thanks the Deutsche Forschungsgemeinschaft for a Deutsch-Israelische Projektkooperation (DIP) Grant and the European Union's Horizon 2020 Research and Innovation Programme Q-SORT (Grant No. 766970 under H2020-FETOPEN-2016-2017). This project has received fund-

ing from the European Union's Horizon 2020 Research and Innovation Programme (Grant No. 823717, project "ESTEEM3").

Supporting Information Available

Supplementary information: Representative off-axis electron hologram, reconstructed phase images, phase contour maps, reconstructed 3D shape of the needle and parameters used for model-based iterative reconstruction.

References

(1) Sze, S. M. Semiconductor devices: Physics and technology; Wiley, 2008.

(2) Zheng, X.; Chen, G.; Li, Z.; Deng, S.; Xu, N. Quantum-mechanical investigation of field-emission mechanism of a micrometer-long single-walled carbon nanotube. Physical Review Letters **2004**, 92, 106803.

(3) Zhang, H.; Tang, J.; Yuan, J.; Yamauchi, Y.; Suzuki, T. T.; Shinya, N.; Nakajima, K.; Qin, L.-C. An ultrabright and monochromatic electron point source made of a LaB_6 nanowire. Nature Nanotechnology **2016**, 11, 273.

(4) Zhou, Y.; Liang, Y.; Fu, J.; Liu, K.; Chen, Q.; Wang, X.; Li, H.; Zhu, L.; Hu, J.; Pan, H.; Miyauchi, M.; Jiang, L.; Cortés, E.; Liu, M. Vertical Cu nanoneedle arrays enhance the local electric field promoting C_2 Hydrocarbons in the CO_2 electroreduction. Nano Letters **2022**, 22, 1963–1970.

(5) Gault, B.; Chiaramonti, A.; Cojocaru-Mirédin, O.; Stender, P.; Dubosq, R.; Freysoldt, C.; Makineni, S. K.; Li, T.; Moody, M.; Cairney, J. M. Atom probe tomography. Nature Reviews Methods Primers **2021**, 1, 51.

(6) Vurpillot, F.; Oberdorfer, C. Modeling atom probe tomography: A review. Ultramicroscopy **2015**, 159, 202–216.

(7) Su, Y.; Liu, C.; Brittman, S.; Tang, J.; Fu, A.; Kornienko, N.; Kong, Q.; Yang, P. Single-nanowire photoelectrochemistry. Nature Nanotechnology **2016**, 11, 609.

(8) Liu, M. et al. Enhanced electrocatalytic CO_2 reduction via field-induced reagent concentration. Nature **2016**, 537, 382.

(9) Lichte, H.; Lehmann, M. Electron holography—basics and applications. Reports on Progress in Physics **2007**, 71, 016102.

(10) Twitchett, A.; Dunin-Borkowski, R.; Midgley, P. Quantitative electron holography of biased semiconductor devices. Physical Review Letters **2002**, 88, 238302.

(11) Twitchett-Harrison, A. C.; Yates, T. J.; Newcomb, S. B.; Dunin-Borkowski, R. E.; Midgley, P. A. High-resolution three-dimensional mapping of semiconductor dopant potentials. Nano Letters **2007**, 7, 2020–2023.

(12) Wolf, D.; Lichte, H.; Pozzi, G.; Prete, P.; Lovergine, N. Electron holographic tomography for mapping the three-dimensional distribution of electrostatic potential in III-V semiconductor nanowires. Applied Physics Letters **2011**, 98, 264103.

(13) Li, L.; Smith, D. J.; Dailey, E.; Madras, P.; Drucker, J.; McCartney, M. R. Observation of hole accumulation in Ge/Si core/shell nanowires using off-axis electron holography. Nano letters **2011**, 11, 493–497.

(14) Wolf, D.; Lubk, A.; Lenk, A.; Sturm, S.; Lichte, H. Tomographic investigation of fermi level pinning at focused ion beam milled semiconductor surfaces. Applied Physics Letters **2013**, 103, 264104.

(15) Wolf, D.; Lubk, A.; Prete, P.; Lovergine, N.; Lichte, H. 3D mapping of nanoscale electric

potentials in semiconductor structures using electron-holographic tomography. Journal of Physics D: Applied Physics **2016**, 49, 364004.

(16) Gan, Z.; Perea, D.; Yoo, J.; He, Y.; Colby, R.; Barker, J.; Gu, M.; Mao, S.; Wang, C.; Picraux, S.; Smith, D.; McCartney, M. Characterization of electrical properties in axial Si-Ge nanowire heterojunctions using off-axis electron holography and atom-probe tomography. Journal of Applied Physics **2016**, 120, 104301.

(17) Chalasani, R.; Pekin, A.; Rabkin, A.; Abutbul, R. E.; Diéguez, O.; Kauffmann, Y.; Golan, Y.; Kohn, A. Mapping charge distribution in single PbS core–CdS arm nanomultipod heterostructures by off-axis electron holography. Nano Letters **2017**, 17, 2778–2787.

(18) Li, L.; Cheng, Y.; Liu, Z.; Yan, S.; Li, L.; Wang, J.; Zhang, L.; Gao, Y. Study of structure-property relationship of semiconductor nanomaterials by off-axis electron holography. Journal of Semiconductors **2022**, 43, 041103.

(19) Cumings, J.; Zettl, A.; McCartney, M.; Spence, J. Electron holography of field-emitting carbon nanotubes. Physical Review Letters **2002**, 88, 056804.

(20) Lubk, A.; Wolf, D.; Simon, P.; Wang, C.; Sturm, S.; Felser, C. Nanoscale three-dimensional reconstruction of electric and magnetic stray fields around nanowires. Applied Physics Letters **2014**, 105, 173110.

(21) Beleggia, M.; Kasama, T.; Larson, D.; Kelly, T.; Dunin-Borkowski, R.; Pozzi, G. Towards quantitative off-axis electron holographic mapping of the electric field around the tip of a sharp biased metallic needle. Journal of Applied Physics **2014**, 116, 024305.

(22) Migunov, V.; London, A.; Farle, M.; Dunin-Borkowski, R. Model-independent measurement of the charge density distribution along an Fe atom probe needle using off-axis electron holography without mean inner potential effects. Journal of Applied Physics **2015**, 117, 134301.

(23) Phatak, C.; De Knoop, L.; Houdellier, F.; Gatel, C.; Hÿtch, M.; Masseboeuf, A. Quantitative 3D electromagnetic field determination of 1D nanostructures from single projection. Ultramicroscopy **2016**, 164, 24–30.

(24) Beleggia, M.; Kasama, T.; Dunin-Borkowski, R. E.; Hofmann, S.; Pozzi, G. Direct measurement of the charge distribution along a biased carbon nanotube bundle using electron holography. Applied Physics Letters **2011**, 98, 243101.

(25) Gatel, C.; Lubk, A.; Pozzi, G.; Snoeck, E.; Hÿtch, M. Counting elementary charges on nanoparticles by electron holography. Physical Review Letters **2013**, 111, 025501.

(26) Gan, Z.; Gu, M.; Tang, J.; Wang, C.-Y.; He, Y.; Wang, K. L.; Wang, C.; Smith, D. J.; McCartney, M. R. Direct mapping of charge distribution during lithiation of Ge nanowires using off-axis electron holography. Nano Letters **2016**, 16, 3748–3753.

(27) Vicarelli, L.; Migunov, V.; Malladi, S.; Zandbergen, H. W.; Dunin-Borkowski, R. E. Single electron precision in the measurement of charge distributions on electrically biased graphene nanotips using electron holography. Nano Letters **2019**, 19, 4091–4096.

(28) Zheng, F.; Caron, J.; Migunov, V.; Beleggia, M.; Pozzi, G.; Dunin-Borkowski, R. E. Measurement of charge density in nanoscale materials using off-axis electron holography. Journal of Electron Spectroscopy and Related Phenomena **2020**, 241, 146881.

(29) Lai, G.; Hirayama, T.; Ishizuka, K.; Tanji, T.; Tonomura, A. Three-dimensional reconstruction of electric-potential distribution in electron-holographic interferometry. Applied Optics **1994**, 33, 829–833.

(30) Simon, P.; Wolf, D.; Wang, C.; Levin, A. A.; Lubk, A.; Sturm, S.; Lichte, H.; Fecher, G. H.; Felser, C. Synthesis and three-dimensional magnetic field mapping of Co2FeGa Heusler nanowires at 5 nm resolution. Nano Letters **2015**, 16, 114–120.

(31) Wolf, D.; Rodriguez, L. A.; Béché, A.; Javon, E.; Serrano, L.; Magen, C.; Gatel, C.; Lubk, A.; Lichte, H.; Bals, S.; Tendeloo, G. V.; Fernández-Pacheco, A.; Teresa, J. D.; Snoeck, E. 3D magnetic induction maps of nanoscale materials revealed by electron holographic tomography. Chemistry of Materials **2015**, 27, 6771–6778.

(32) Wu, M.; Tafel, A.; Hommelhoff, P.; Spiecker, E. Determination of 3D electrostatic field at an electron nano-emitter. Applied Physics Letters **2019**, 114, 013101.

(33) Lade, S. J.; Paganin, D.; Morgan, M. J. Electron tomography of electromagnetic fields, potentials and sources. Optics Communications **2005**, 253, 392–400.

(34) Mohan, K. A.; Prabhat, K.; Phatak, C.; De Graef, M.; Bouman, C. A. Iterative reconstruction of the magnetization and charge density using vector field electron tomography. Microscopy and Microanalysis **2016**, 22, 1686–1687.

(35) Matteucci, G.; Missiroli, G.; Muccini, M.; Pozzi, G. Electron holography in the study of the electrostatic fields: the case of charged microtips. Ultramicroscopy **1992**, 45, 77–83.

(36) Caron, J. Model-based reconstruction of magnetisation distributions in nanostructures from electron optical phase images. Ph.D. thesis, RWTH Aachen University, 2017.

(37) Oikawa, T.; Kim, J. J.; Tomita, T.; Park, H. S.; Shindo, D. Measurement of electric potential distributions around FEG-emitters by electron holography. Journal of Electron Microscopy **2007**, 56, 171–175.

(38) Mandal, S.; Pradeep, K. G.; Zaefferer, S.; Raabe, D. A novel approach to measure grain boundary segregation in bulk polycrystalline materials in dependence of the boundaries' five rotational degrees of freedom. Scripta Materialia **2014**, 81, 16–19.

(39) Volkov, V.; Han, M.; Zhu, Y. Double-resolution electron holography with simple Fourier transform of fringe-shifted holograms. Ultramicroscopy **2013**, 134, 175–184.

(40) Ru, Q.; Lai, G.; Aoyama, K.; Endo, J.; Tonomura, A. Principle and application of phase-shifting electron holography. Ultramicroscopy **1994**, 55, 209–220.

(41) van Aarle, W.; Palenstijn, W. J.; De Beenhouwer, J.; Altantzis, T.; Bals, S.; Batenburg, K. J.; Sijbers, J. The ASTRA Toolbox: A platform for advanced algorithm development in electron tomography. Ultramicroscopy **2015**, 157, 35–47.

(42) Jackson, J. Classical Electrodynamics; Wiley, 1998.

(43) Tsong, T. Field penetration and band bending near semiconductor surfaces in high electric fields. Surface Science **1979**, 81, 28–42.

(44) Zheng, F.; Pozzi, G.; Migunov, V.; Pirker, L.; RemÅ¡kar, M.; Beleggia, M.; Dunin-Borkowski, R. E. Quantitative measurement of charge accumulation along a quasi-one-dimensional W_5O_{14} nanowire during electron field emission. Nanoscale **2020**, 12, 10559–10564.

(45) Du, S.; Burgess, T.; Tjing Loi, S.; Gault, B.; Gao, Q.; Bao, P.; Li, L.; Cui, X.; Kong Yeoh, W.; Hoe Tan, H.; Jagadish, C.; Ringer, S. P.; Zheng, R. Full tip imaging in atom probe tomography. Ultramicroscopy **2013**, 124, 96–101.

(46) Loi, S. T.; Gault, B.; Ringer, S. P.; Larson, D. J.; Geiser, B. P. Electrostatic simulations of a local electrode atom probe: The dependence of tomographic reconstruction parameters on specimen and microscope geometry. Ultramicroscopy **2013**, 132, 107–113.

(47) Morgan, P. Carbon fibers and their composites; CRC press, 2005.